ORIGINAL CONTRIBUTION

Exploring Possibilities for Fabricating Cu–TiB$_2$ Composite Through Different Powder Metallurgy Routes

Uttam Kumar Murmu[1] · **Shrishty Sahu**[1] ·
Abhishek Ghosh[1] · **Manojit Ghosh**[1]

Abstract Achievement of the most desirable mechanical properties through smooth processing techniques has led to the development of composite materials for sustainable applications. Powder metallurgy (PM) finds a special area of interest in fabricating composite materials among several processing strategies. Introduction of nano-TiB$_2$ particles in Cu matrix through in situ or ex-situ processing is recently addressed to achieve a good combination of strength and conductivity. In this present investigation, Cu and TiB$_2$ powders (5 wt%) were subjected to ball milling and subsequently manufactured through three different powder metallurgy routes, i.e., hot pressing (HP), spark plasma sintering (SPS), and equal channel angular pressing (ECAP). A conventional PM route through simultaneous pressing and sintering (HP) is being compared with a severe plastic deformation (SPD) process (ECAP), while SPS operates with a completely different principle. This article guides toward the pros and cons of the three different processing routes in terms of relative density, porosity, hardness, strain, and the microstructure has been revealed through optical microscopy, field emission scanning electron microscopy, and X-ray diffraction. Transmission electron microscopy for the TiB$_2$ particles was performed to ensure the particle size and dynamic light scattering for particle size distribution. Among all the three processing routes, the samples consolidated through SPS were found to possess the best relative density (~ 97.5%), microhardness (~ 142 Hv), and strain (~ 0.269), followed by ECAP and HP samples. A comparison of the grain refinement mechanism of the composites processed through different routes has also been presented.

Keywords Powder metallurgy · Hot pressing · Equal channel angular extrusion · Spark plasma sintering

Introduction

Cu-based composites have been a topic of great interest among researchers worldwide for the last 20 years. It has gained much popularity due to its various applications in the electronic and manufacturing industries, especially in the production of sliding contact bearings, motor bushes, welding electrodes, machine housings, heat sinks, substrates, etc. [1, 2] that require microstructural stability at high temperatures in addition to sound mechanical and electrical properties [3, 4]. Furthermore, adding ceramic or compound materials to the Cu matrix as reinforcements to ensure better mechanical properties (such as stiffness, toughness, ambient, and high-temperature strength) is not unheard of [5, 6]. Such reinforcements may include particulates, continuous and discontinuous fibers, and/or whiskers [7]. Several attempts have been made in the last few years to reinforce the Cu matrix by dispersing particles like oxides, carbides, or borides through powder metallurgy or melt-casting routes [8-10]. The addition of titanium diboride (TiB$_2$) either by in situ or ex-situ processes into the Cu matrix has been reported to be a promising route in improving the desired properties of the composite, like stiffness, hardness, and wear resistance, along with a decrease in its coefficient of thermal expansion (CTE) [11-15]. Moreover, the high melting point (3253 K),

✉ Abhishek Ghosh

✉ Manojit Ghosh
mghosh.metal@faculty.iiests.ac.in

1 Department of Metallurgy and Materials Engineering, Indian Institute of Engineering Science and Technology, Shibpur, Howrah 711103, India

248

J. Inst. Eng. India Ser. D (January–June 2023) 104(1):247–257

low density (4.52 g/cm^3), high thermal (25 W/m·K), and electrical conductivity ($9 \times 10^{-8}\Omega$m) of TiB$_2$ make it a superior reinforcing material for Cu. However, the formation of in situ TiB$_2$ inside the Cu matrix through the conventional powder metallurgy route (pressing followed by sintering) demands precise control over the processing parameters, which contributes to the complicacy of the process. Various properties of Cu–TiB$_2$ composites can be achieved by varying the degree of reinforcement (% of TiB$_2$ in Cu matrix), thereby making the composites suitable for any typical applications. Also, the processing techniques (powder metallurgy, melting and casting technique, etc.) govern the physical properties and microstructures obtained in the composites [16]. Several researchers [17-19] have reported a high value of relative density, uniform distribution of reinforcement particles, and moderate hardness values with an addition of 5 wt% TiB$_2$. Zongning Chen et al. [17] achieved a 140% improvement in the UTS value without compromising its ductility concerning the Al matrix. Chidambaram et al. [18] also studied the microstructure and mechanical properties of AA6061–5 wt.%TiB$_2$ in situ metal matrix composite subjected to equal channel angular pressing. They showed excellent grain refinement and high strain with increased mechanical properties. Abdollah Bahador et al. [19] also demonstrated remarkable strengthening while sustaining a considerable elongation using 5 wt%TiB$_2$. Promising results have also been reported with Cu-5%TiB$_2$ reinforcement particles, although in all of the cases, the formation of TiB$_2$ has been controlled in an in situ manner [20, 21]. An effort has been made to investigate the effect in properties by adding TiB$_2$ through an ex-situ mechanism, maintaining the same composition, which has delivered the best results.

The powder metallurgy route, in particular, is capable of synthesizing a wide variety of compositions and generating more complex shaped composites with controlled porosity as compared to the orthodox melting and casting route. Some of the well-known powder consolidation processes include hot pressing (HP), spark plasma sintering (SPS), and equal channel angular pressing (ECAP). The HP technique involves the deformation of the powder mixture through creep and material transfer by being pressed into a die at high temperatures. Here, the heat transfer rate between the die and the sample is low, which causes the process to last even for hours. The SPS process, also known as field-assisted sintering technique (FAST) or pulsed electric current-assisted sintering (PECAS), is just a variant of HP in which a pulsed DC current is passed through the powder mixture, which in turn acts as the heat source. It is a well-known and well-established technique that efficiently produces high-density powder metallurgy components in a shorter sintering time than conventional techniques. Furthermore, SPS can be used to complete the densification of many materials that are typically difficult to sinter using other conventional processes

[22]. However, the non-homogenous distribution of temperature is one of its drawbacks. In contrast, the ECAP process is a deformation technique that produces ultrafine grains by passing the composite powder through an angular die. It was first presented as a shaping cycle in which high strain was forced into the metal by basic shear. It has become a significant handling method for refining microstructure in metallic materials through the severe plastic deformation (SPD) process [23]. A high degree of homogeneity might be accomplished through the ECAP technique when the number of ECAP passes is large enough. However, the degree of homogeneity achieved in ECAP also relies upon the solidifying qualities of the material. Handling by ECAP prompts huge reinforcing of the material at surrounding temperature and gives the ultrafine grains sensible thermal stability at high strain rates. Among the processes mentioned above, SPS and ECAP offer outstanding densification and matrix-reinforcement bonding over HP, thereby developing excellent mechanical properties [24]. The SPS samples exhibit low porosity and high strength, revealing better bonding of matrix – reinforcements. Thus, this work aims to report a comparative study among HP, SPS and ECAP performed at 500 °C for TiB$_2$ reinforced Cu matrix and judge the best-suited process in terms of development of microstructure leading toward the exhibition of the best properties among these composites.

Materials and Methods

Details of as-Received Powders

The starting materials for the three processes chosen for the present investigation are Cu and TiB$_2$ powders. The details of the as-received powders are presented in Table 1.

Figure 1 represents the SEM microstructure of the as-received elemental powders. It can be seen that pure Cu powder is dendritic in shape, while TiB$_2$ powder has a hexagonal or irregular shape when coagulated. Clearly,

Table 1 Description of as-received powders

Powder	Cu	TiB$_2$
Company	Loba Chemie	Intelligent Materials Pvt. Ltd
Purity	99.9%	99.9%
Color	Reddish brown powder	Grey
Particle size	−45 micron	<80 nm
Melting point (°C)	1083	3230
Density (g/cm3)	8.94	4.52
Molecular weight (g/mol)	63.55	69.489
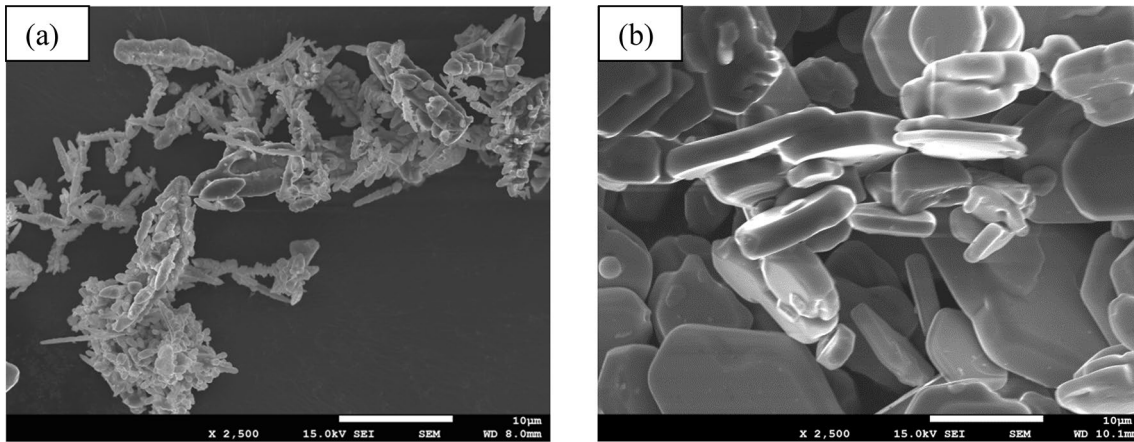
**Fig. 1** SEM micrograph of as-received **a** Cu and **b** TiB$_2$ powders
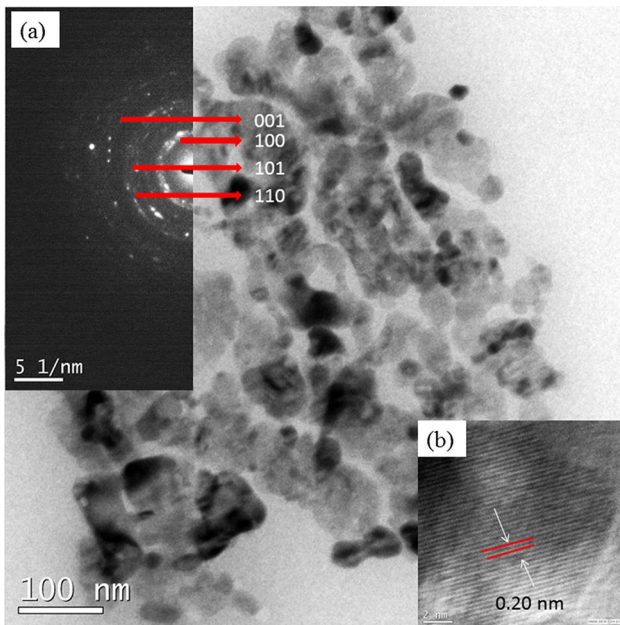
Fig. 2 TEM micrograph of as-received TiB$_2$ nano powder **a** SAED pattern **b** lattice fringes

transmission electron microscopy (TEM) would be a better technique for revealing the size and shape of the TiB$_2$ powder.

Figure 2 represents the TEM micrograph of as-received TiB$_2$ nano powder with (a) corresponding SAED and (b) lattice fringes. The micrograph exhibits that TiB$_2$ is polycrystalline, having numerous single nanoparticles around the structure. The size of the nanoparticles is proved to be quite prominent according to the dynamic laser scattering (DLS) method, as it is measured to be less than 80 nm (Fig. 3). SAED pattern characteristics consisted of multiple rings that were indexed as (001), (100), (101), and (110). This further supported the fact that the as-received nano-powders were polycrystalline. These polycrystalline structures demonstrated a direct view of the hexagonal lattice structure, which is in good agreement with the atomic model of TiB$_2$, consisting of a hexagonal arrangement of Ti and B atoms [25].

The dynamic laser scattering (DLS) method, previously known as Photon Correlation Spectroscopy (PCS) or Quasi-Elastic Light Scattering (QELS), is an efficient and powerful tool for characterizing the particle size as well as particle size distribution under Brownian motion [26] in a
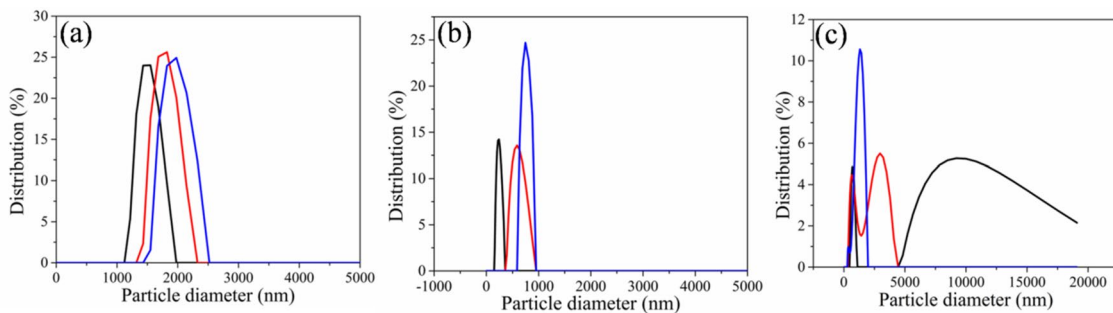
Fig. 3 DLS study of the raw materials of **a** Cu, **b** TiB$_2$, and **c** milled powder

suitable solution. It is a simple, non-destructive, and minimal expense method, and its activity is moderately straightforward and quick [27]. This study used the DLS technique with Litesizer 500 instrument at RT. The recorded data were taken by ISO particle size analysis mode using water as a solvent with a refractive index of 1.3302 and viscosity of 0.8863 mPa.s.

The particle size distribution of the as-received samples (Cu, TiB$_2$) and the milled powders were analyzed by the DLS technique. The results showed strong evidence of the particle size curves being a function of distribution percentage, especially with the peaks becoming narrower (Fig. 3). The results also showed that the particle size of Cu was in the range of 1.5–3 μm, TiB$_2$ was near about 100 nm to 1 μm, and the milled powder had the size of about 100 nm to 5 μm. The particle size of Cu powder being within the micron range and TiB$_2$ being in the nanorange declares the data from the manufacturer to be trustworthy.

The results achieved can be reasoned with (a) the dispersion of the powders in water is improper due to the low solubility of metal powders, (b) metal powders have a higher density (c) this technique reflects the fact that the direction-based size analysis provides the diameter of the coherently scattered grains by lightweight scattering or imaging methods, but in this case, the powders were found to have an irregular shape.

Ball Milling

The intended composition of powder mixtures between Cu and TiB$_2$ (5 wt% TiB$_2$) was achieved through ball-milling using a planetary ball-mill (FRITSCH, Planetary Mono Mill PULVERISETTE 6). Tungsten carbide balls (35 in number), each weighing 10 gm and possessing a diameter of 10 mm, were used inside a tungsten carbide vial. The ball-to-powder weight proportion was maintained at 20:1. Dry millings of the mixtures were performed at a speed of 300 rpm, and milling was continued for 26 h. Finally, a vacuum furnace was used at 50 °C for 30 min to dry and overcome the stiffness of the powder mixture.

The Fabrication Processes

The milled powders were subjected to three different consolidation processes, e.g., hot compaction, SPS, and ECAP.

For hot compaction, the powders were loaded into the hot compaction chamber and compacted at 500 °C with a constant pressure of 20 tonnes, keeping a holding time of 2 min. Finally, the compacts were cooled by compressed air. The hot compaction technique combines the effect of pressing and sintering the powder in a controlled environment while retaining dimensional precision. For the hot pressing (HP) operation, a hydraulic pump and graphite resistors inside the graphite molds were used to manage the pressure. A schematic description of the process is represented in Fig. 4a. After the evacuation process, the chamber was filled with nitrogen and heated at 10 K/min. The pressure was increased to 20 tonnes and sustained for 2 min after reaching the required temperature. The samples were then air-cooled before being used for optical microscopy (OM), scanning electron microscopy (SEM), and X-ray diffractometer (XRD).

Spark plasma sintering (SPS) was performed at International Advanced Research Centre for Powder Metallurgy and New Materials Department (ARCI, Hyderabad) with SCM 1050 machine manufactured by Sumitomo Coal Mining Co,
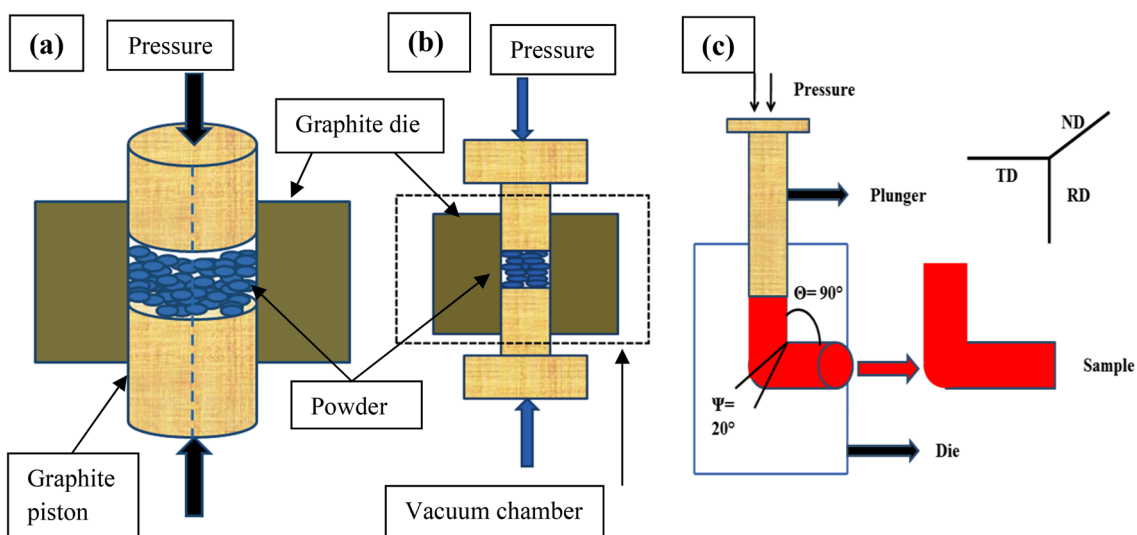

Fig. 4 Schematic diagram of **a** HP **b** SPS and **c** ECAP processes

Ltd Japan. A 20 mm graphite die was used to conduct the SPS technique, and a uniaxial pressure of 70 MPa [28] was applied with an inert Argon atmosphere. A heating rate of 90 °C/min was used during consolidation, and the samples were held at 500 °C for 15 min. The surface impurities that caused contamination were then removed by grinding all the samples in graphite dies. A schematic description of the process is represented in Fig. 4b.

The ECAP process was carried out by putting the powder mixture inside a Cu can, thus ensuring its consolidation. The inner diameter and height of the can were 11.9 and 60 mm, respectively. The ECAP process was carried out at 500ºC using a muffle furnace. In the furnace, the Cu can filled with milled powder was left for 1 h and subsequently introduced straight away into the ECAP chamber for consolidation with a pressure of 15 tons. The mixed powders were pressed through route A by using an ECAP die that had a horizontal and a vertical channel converging at an angle of $\theta = 90°$ with a curvature at the corner angle of $\Psi = 20°$ (Fig. 4c). Moreover, MoS_2 lubricant was used to reduce the friction between the samples and punch and die channel surface during the process. It must be noted that the height and the diameter of the die channels were 126 mm and 12.3 mm, respectively. Fig. 5 represents the shape of the consolidated samples after each powder metallurgy route. Quite naturally the samples appeared disc shaped afte HP (Fig. 5a) and SPS (Fig. 5b), while cylindrical after ECAP (Fig. 5c)

Characterization of the Composite After Consolidation

The compacts, after fabrication, were sectioned by an electrical discharge machining (EDM) machine to reveal the section of interest for microstructural investigation (Fig. 6). Grinding was followed by paper polishing (200–1200 grit SiC particle-based emery papers), cloth polishing (velvet cloth), diamond polishing (by 0.5–1 μm diamond paste), and finally etching (mixing of ammonia solution, distilled water, and hydrogen peroxide (3%) in a volume ratio of 1:1:2) for 10 s by swabbing to reveal the microstructure under optical microscopy (Leica, DM6 FS). The phases present were analyzed with an X-ray diffractometer (Bruker, D8 ADVANCE). The XRD data that revealed various phases present in the
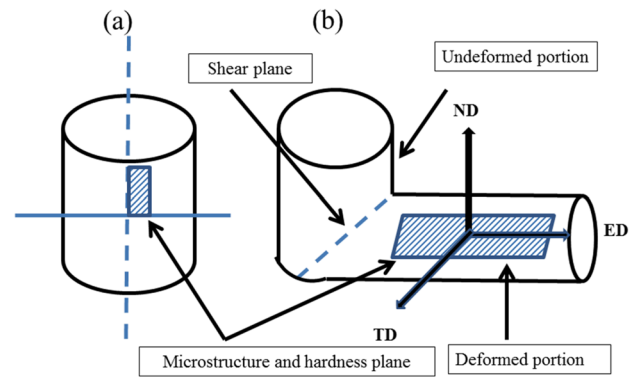

Fig. 6 Schematic area of the sample unveiling microstructure and hardness planes

structure were obtained using copper Kα radiation having a wavelength of 0.15408 nm, within a scan range of 10 to 100º and at a scan rate of 0.02° per second. SEM (JEOL JSM-7610F FEG-SEM) was used for microstructural analysis. Mechanical characterization in the form of microhardness tests was also conducted by applying a load of 200 gf for 15 s dwell time by INNOVATEST VERZUS 750 CCD Universal Hardness Tester. A minimum of 7 data points were recorded with a confidence index of 0.92 and an accuracy of $\pm 2\%$ to calculate the average hardness.
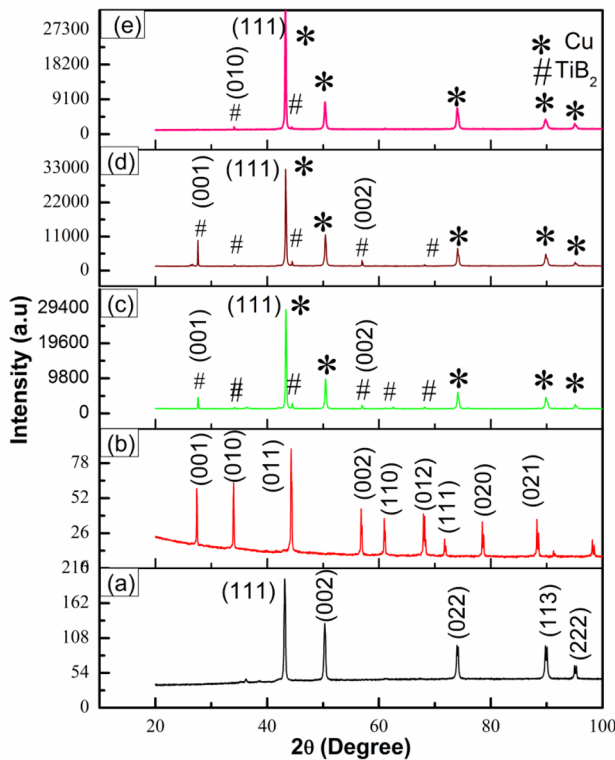
Results and Discussion

Revealing Phases of the Composites by X-ray Diffraction

Figure 7 shows the XRD pattern for the initial powders and composites consolidated through different processing routes. The XRD data revealed only the presence of Cu and TiB_2 phases in the structure, indicating the absence of any chemical reaction between the matrix and the reinforcement. However, the orientations of the domains were different typically for TiB_2 particles, and the most plausible explanation lies in the difference in strain mode for the three different fabrication routes. The sample processed through ECAP recorded
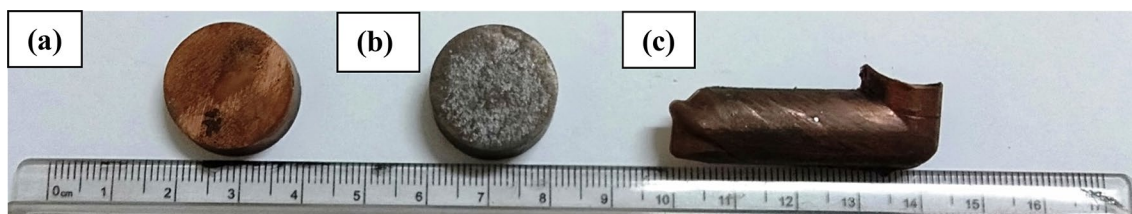
Fig. 5 Real images of consolidated samples through **a** HP, **b** SPS, and **c** ECAP processes

252

J. Inst. Eng. India Ser. D (January–June 2023) 104(1):247–257

Fig. 7 X-ray diffraction data of **a** pure Cu, **b** TiB$_2$, **c** HP, **d** SPS, and **e** ECAP-ed sample

Fig. 8 Calculated micro-strain (ε) versus 2θ of the composite processed through different processing routes
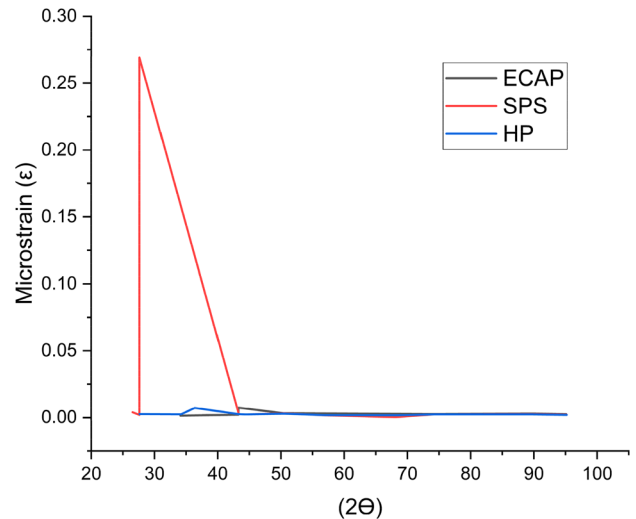
the absence of (001), (002), (110), and (012) peaks for TiB$_2$ particles as compared to the other two processes. Similarly, for the SPS samples, (110) orientation was found absent. In the case of an SPS sample, the TiB$_2$ phase was more prominent than the other two processing routes. This can be reasoned with high strain values and fine particles in the structure, which imposed a high level of strain in a short duration of time with sufficient activation energy [29] to accelerate the formation of TiB$_2$ phases.

Development of Strain After Different Consolidation Processes

XRD is a crucial technique that can determine strain development during the consolidation process after analyzing the XRD peak profiles. The factors responsible for strain are non-uniform lattice distortions, dislocations, antiphase domain boundaries, etc. The most accepted equation used for the calculation of strain is as follows [30]:

$$\varepsilon = \frac{\beta}{4 \tan \theta} \tag{1}$$

where ε is the strain, β is the line broadening at FWHM (full width at half maximum), and θ is Bragg's angle (all values

are in radians). It is noteworthy that strain is considered the only responsible factor for XRD peak broadening. The line broadening at FWHM of the profile was found by multiple peak fitting and was then substituted in the formula to find the strain. Subsequently, a graph was plotted for ε versus 2θ values for all the three fabrication processes.

Figure 8 represents the micro-strain (ε) versus 2θ values of the composite after undergoing ECAP, SPS, and HP processes. From this, it can be inferred that the strain developed in SPS processed composites is the highest, followed by ECAP and HP processes for low values of 2θ. However, the strain developed for higher values of 2θ is almost the same for all the processes. SPS processed composites consist of smaller crystallite sizes due to which larger micro-strains were present in the compact because the value of strain is higher for more refined grains [31]. The reduction in crystallite size may be due to subgrain formation, dislocation, and grain boundary sliding that happened in the materials while the heterogeneous debris interacted and their atoms tried to diffuse for the duration of the SPS system due to the applied heat and sintering pressure.

Table 2 Porosity % of the samples processed through HP, ECAP, and SPS

Sample	Weight in wet air (gm)	Weight in dry air (gm)	Weight in water (gm)	Porosity (%)
HP	13.93412	13.91991	11.84641	0.68
SPS	21.59841	21.59608	18.91324	0.087
ECAP	5.66412	5.66333	5.03681	0.126

**Porosity Measurement and Change Density**

Porosity is a fundamental physical quantity strongly related to other mechanical properties, such as fatigue life, tensile strength, and ductility [32, 33]. Pores act as stress concentrators that degrade a component's mechanical strength and life and introduce variations in mechanical test results. In the present work, an attempt has been made to measure the open porosity (in % of voids or pores) present in the composite surfaces by the water absorption method (NF P 18-459 standard). The porosity measurements involve the removal of water from the pores and subsequently filling the same with a suitable fluid using the formula (equation 2):

$$\%\text{Porosity} = \frac{\text{Weight in wet air} - \text{weight in dry air}}{\text{Weight in wet air} - \text{weight in water}} \times 100\%$$

(2)

Samples processed by HP possessed the highest porosity (0.68%) level, while the SPS samples had the lowest (0.087%) amount (Table 2). These results confirmed that the SPS process is the most promising consolidation process as the voids created during sintering in terms of trapped air or trapped volatile gas were removed. The plasma activation stage in sintering can explain the low porosity, which incorporates a higher diffusion rate, hot pressing, resistance heating, and the high-frequency pulse current between the atomized powder particles [34].

The compacts' relative densities were calculated using Archimedes' principle to substantiate the porosity experiment, according to ASTM B962–08 [35]. The relative densities of these composites were calculated in agreement with the linear rule of mixture, considering the theoretical densities of Cu and TiB_2 as 8.96 g/cm^3 and
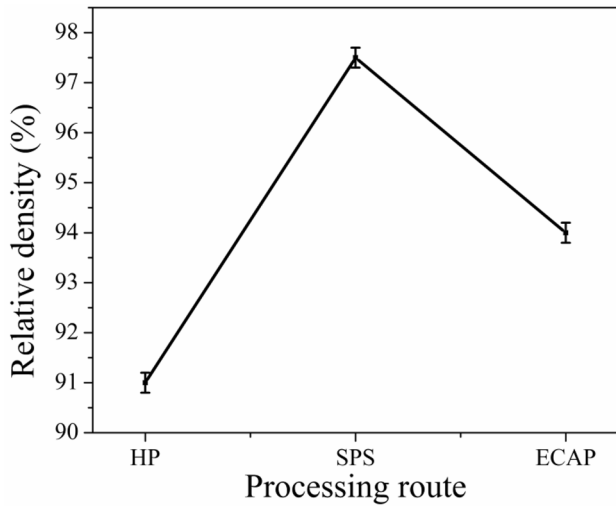
Fig. 9 Relative density of the composites after consolidation through different processing routes

Fig. 10 Optical micrographs of **a** HP, **b** SPS, and **c** ECAP-ed sample

254

J. Inst. Eng. India Ser. D (January–June 2023) 104(1):247–257
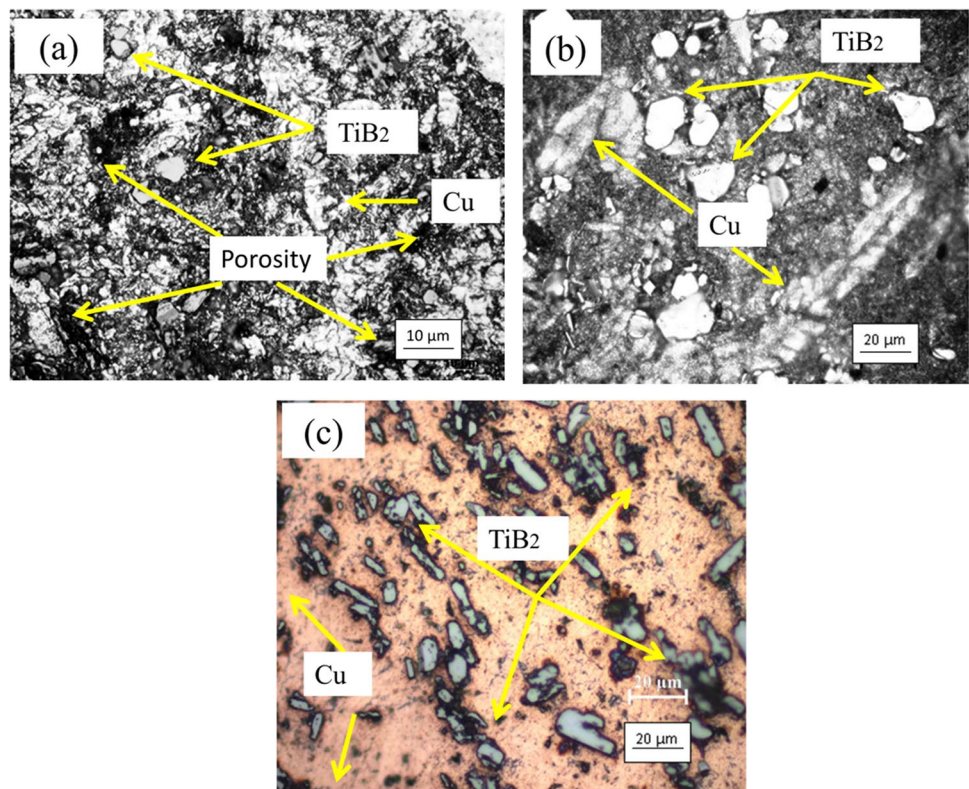
7.76 g/cm^3, respectively. From Fig. 9, it can be concluded that the relative density achieved is in the sequence of SPS > ECAP > HP, with the highest appearing first. SPS is a decent way to deal with sinter materials, particularly those with lower sinterability. High-energy plasma can achieve a few peculiarities that can upgrade densification, for example, particle surface initiation, neighborhood or local dissolving, and dissipation on the outer layer of the powder particles, which instigate neck arrangement between particles. The SPS interaction makes it conceivable to sinter diboride-based materials (ZrB_2, HfB_2, and TiB_2) at a lower temperature and in a more limited time contrasted to the other conventional processes like HP [36, 37]. On the other hand, effective densification of powder could be achieved through SPS due to Joule heating and electric field diffusion [38, 39]. This approach usually is suitable for consolidating nano-powders without allowing enough time for grain growth. Therefore, it may be concluded that SPS is a promising approach to obtaining high-density composites.

Microstructure of the Composites

The microstructure of the composites was revealed through OM and SEM and the compositions at different places were traced by energy-dispersive X-ray spectroscopy (EDS).

The macrostructure of the metal-matrix composites of the HP, SPS, and ECAP is shown in Fig. 10a, b and c, respectively. The nano-sized TiB_2 particles were coagulated and subsequently dispersed throughout the Cu matrix. Metal matrix composites processed through SPS (Fig. 10b) seem to be well bonded and clean with little trace of porosity. Moreover, the uniform dispersion of strengthening particles within the matrix, better matrix–reinforcement bonding, and grain size refinement are the predominant causes for improving the mechanical properties in an SPS processed sample [40]. The alignment of grains along the ECAP direction is evident from the OM.

Figure 11 shows the micrographs (SEM) of as-sintered materials obtained through various processing routes. The homogeneous distribution of the reinforcing elements can be depicted throughout the Cu matrix for the SPS process.
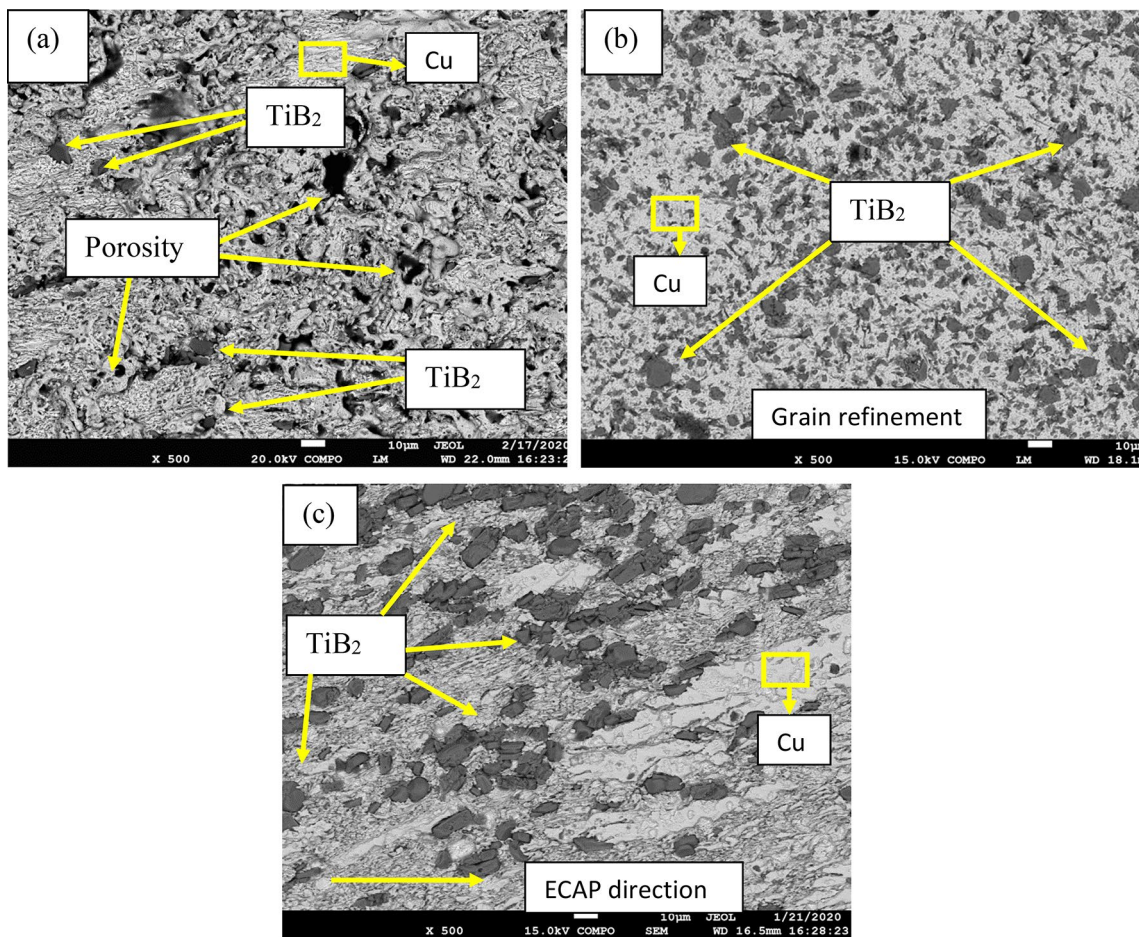
**Fig. 11** SEM micrograph of **a** HP, **b** SPS, and **c** ECAP-ed sample
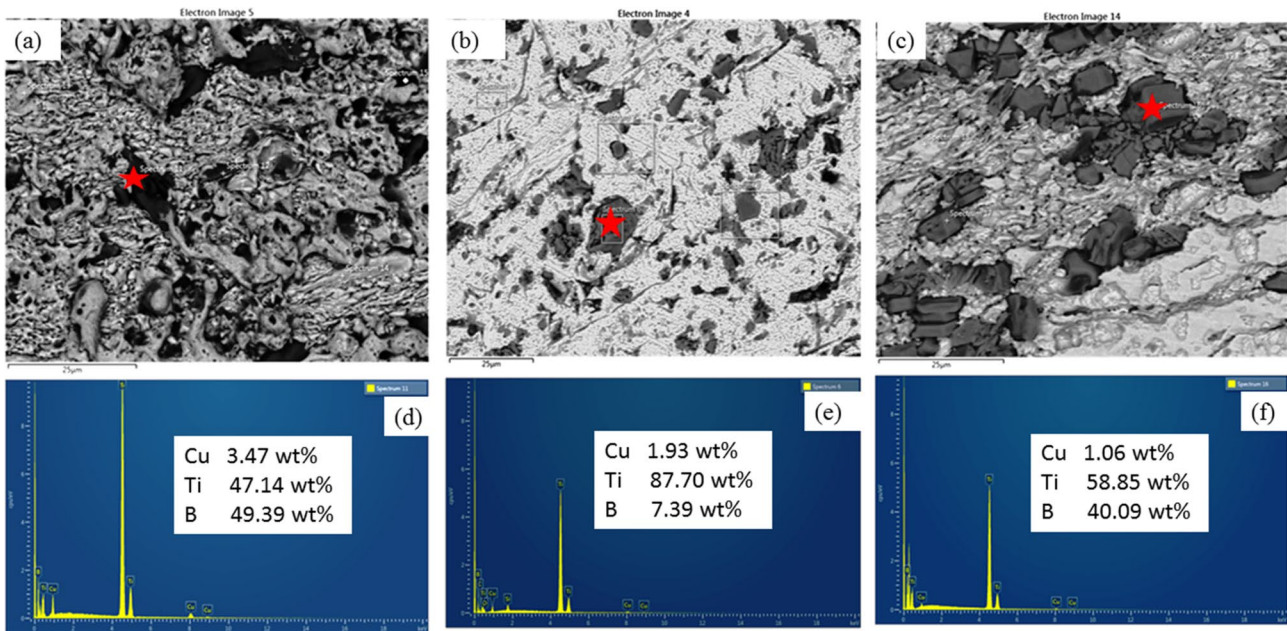
Fig. 12 EDS micrograph of **a** HP, **b** SPS, and **c** ECAP-ed sample

The absence of porosity also ensures a more excellent interfacial bonding between the matrix and the reinforcements [41]. This is a result of the exceptional qualities of the powder metallurgy route that produces materials with a uniform dispersion of different components. The SPS surface shows reduced porosity and better grain refinement compared to HP and ECAP-ed samples, which supports the highest values of hardness for SPS samples. The optical micrographs corroborated the improved bonding between the matrix and the reinforcement improvised by reduced porosity and voids during SPS. The oxide patches are significantly reduced in the case of both SPS and ECAP, as shown in Fig. 12b and c, respectively. These results signify the improved microstructure in terms of grain refinement and homogeneous particle size distribution of the SPS surface in comparison with the other routes.

Impact of Fabrication Routes on the Hardness

Among the three processing routes, the average hardness is the maximum for the SPS process (Fig. 13). The reported average hardness values are achieved after seven tests avoiding elastic interference from each indentation. A greater degree of pore elimination and consequent increase in density can be held responsible for achieving the highest microhardness values for this process [42]. The impact of less porosity is further escalated by the predominant presence of high-density sintered composites. The grain of α- copper is believed to be responsible for the decrease in
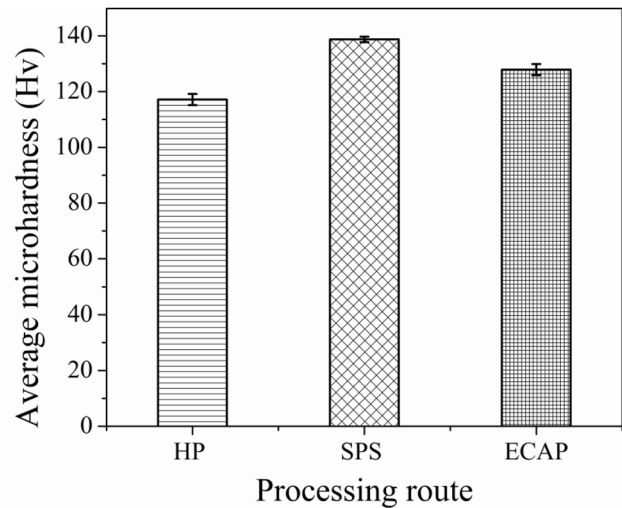
Fig. 13 Average microhardness of the composites through different routes

microhardness of the HP sample. Theoretically, the hardness of the composite should be uniform from one end to the other. However, due to the non-uniform distribution of reinforcement particles in combination with varied load applied across the cross sections at the time of consolidation, the values of hardness obtained at different portions on the surface were different (cf. Figure 14). However, several other factors like cooling rate, gravity, and/or non-uniform distribution of the reinforcement particles in the matrix have led to some discrete values of hardness.

256

J. Inst. Eng. India Ser. D (January–June 2023) 104(1):247–257
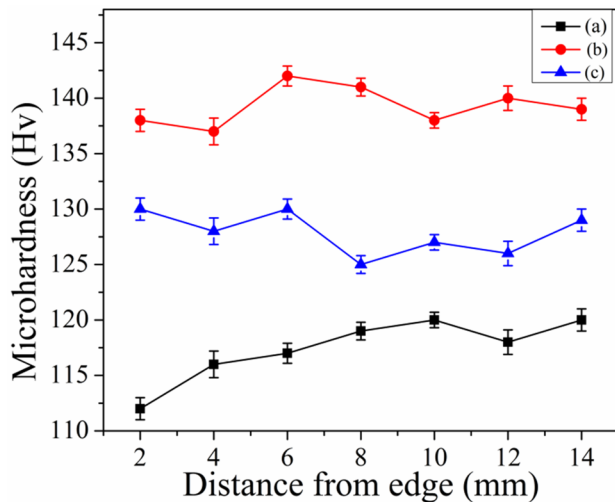
Fig. 14 Microhardness as a function of distance from the edge of the composites for different routes **a** HP, **b** SPS, and **c** ECAP-ed route

Conclusions

Composites with 5 wt% TiB_2 particles in Cu matrix were fabricated through three different processing routes, i.e., HP, SPS, and ECAP, and the properties of the compacts were compared. From the article, the following conclusions can be drawn:

- The initial powders were characterized through SEM, TEM, and DLS. SEM has been used to identify the shape of the particles, TEM to reveal the degree of crystallinity, and DLS for particle size distribution. Among the three different routes, SPS was the most promising route for developing composite materials in the light of density and matrix–reinforcement bonding.
- The samples processed through SPS exhibited better microhardness than ECAP and HP samples due to higher relative density and grain refinement, as evident from the FESEM micrographs.
- XRD data revealed that the sample processed through SPS exhibited the highest intensity of the TiB_2 phase, while the other processes contained Cu and TiB_2 phases in equal proportions.
- SPS processed composites developed the highest amount of strain, followed by ECAP and HP processes which have been held responsible for the increased hardness of the composite.

Declarations

References

1. J. R.davis, Powder Metallurgy: Copper and Copper Alloys,1st edn. (ASM International, Materials Park, OH, 2001), pp. 105-120
2. K. Holmberg, A. Matthews, Coatings tribology; Properties, mechanisms, techniques and applications in surface engineering, Tribology and Interface Engineering, Series 56, 2nd edn. (Elsevier Science, Amsterdam; Boston, 2009), pp. 560
3. S.G. Fishman, Interfaces in composites. J. Met. **38**, 26 (1986)
4. V.C. Nardone, K.W. Prewo, On the strength of discontinuous silicon carbide reinforced aluminum composites. Scr. Metall. **20**, 43 (1986)
5. J.G. Baetz, Metal matrix composites: their time has came. Aerospace America, November, **26,** 14–16 (1998)
6. K.K. Chang, S. Lee, S.Y. Shin, D.H. Kim, Microstructure and properties of Al-based metal matrix composites reinforced by Al60Cu20Ti15Zr5 glassy particles by high pressure hot pressing consolidation. Mat. Sci. Eng. A. **449**, 924-928 (2007)
7. R.H. Palma, H. Sepulveda, A. Aquiles, R. Espinoza, R.C. Montiglio, Performance of Cu–TiC alloy electrodes developed by reaction milling for electrical-resistance welding. J. Mater. Process. Technol. **169**, 62 (2005)
8. S. Semboshi, T. Al-Kassab, R. Gemmab, R. Kirchheim, Ultramicroscopy **109**, 593–598 (2009)
9. S. Nagarjuna, M. Srinivas, K. Balasubramanian, D.S. Sarma, On the variation of mechanical properties with solute content in Cu-Ti alloys. Mater. Sci. Eng. A **259**, 34–42 (1999)
10. G. Song, B. Johannesson, S. Hapugoda, D. St, John, Galvanic corrosion of magnesium alloy AZ91D in contact with an aluminium alloy, steel and zinc. Corros. Sci **46**, 955 (2004)
11. S.C. Tjong, Z.Y. Ma, Microstructural and mechanical characteristics of in situ metal matrix composites. Mater. Sci. Eng. R **29**, 49–113 (2000)
12. Z.Y. Ma, S.C. Tjong, High temperature creep behavior of in-situ TiB_2 particulate reinforced copper-based composite. Mater. Sci. Eng. A **284**, 70–76 (2000)
13. P. Yih, D.D.L. Chung, Titanium diboride copper-matrix composites. J. Mater. Sci. **32**, 1703–1709 (1997)
14. S. Yilmaz, D.C. Dunand, Finite-element analysis of thermal expansion and thermal mismatch stresses in a Cu–60vol%ZrW_2O_8 composite. Compos. Sci. **64**, 1895–1898 (2004)
15. R.N. Caron, Copper: alloying, in Encyclopedia of Materials: Science and Technology, 2nd edn. (Elsevier, Amsterdam, The Netherlands, 2001), pp. 1652–1660 https://doi.org/10.1016/B0-08-043152-6/00289-8
16. A. Fedrizzi, Production of steel matrix composites by mechanical milling and spark plasma sintering, (Doctoral dissertation, University of Trento) (2013)
17. Z. Chen, T. Wangn, Y. Zheng, Y. Zhao, H. Kang, L. Gao, Development of TiB_2 reinforced aluminium foundry alloy based in situ composites-part I: an improved halide salt route to fabricate Al–5 wt%TiB_2 master composite. Mater. Sci. Eng. A **605**, 301–309 (2014)
18. A. Chidambaram, S. Balasivanandha Prabu, K.A. Padmanabhan, Microstructure and mechanical properties of AA6061–5wt.

%TiB2 in-situ metal matrix composite subjected to equal channel angular pressing. Mater. Sci. Eng. A **759**, 762–769 (2019)

19. A. Bahadora, J. Umedaa, R. Yamanoglub, H. Ghandvarc, A. Issariyapata, T. Asma, A. Bakarc, K. Kondoha, Deformation mechanism and enhanced properties of Cu–TiB$_2$ composites evaluated by the in-situ tensile test and microstructure characterization. J. Alloys Compd. **847**, 156555 (2020). https://doi.org/10.1016/j.jallcom.2020.156555

20. Y. Jiang, C. Wang, S. Liang, J. Ren, X. Du, F. Liu, TiB$_2$(-TiB)/Cu in-situ composites prepared by hot-press with the sintering temperature just beneath the melting point of copper. Mater. Charact. **121**, 76–81 (2016)

21. J.H. Kima, J.H. Yuna, Y.H. Park, K.M. Choa, I.D. Choi, I.M. Park, Manufacturing of Cu–TiB2 composites by turbulent in situ mixing process. Mater. Sci. Eng. A **449–451**, 1018–1021 (2007)

22. A. Bahador, E. Hamzah, K. Kondoh, T.A. AbuBakar, F. Yusof, H. Imai, S.N. Saud, M.K. Ibrahim, Effect of deformation on the microstructure, transformation temperature and superelasticity of Ti-23 at% Nb shape-memory alloys. Mater. Des. **118**, 152–162 (2017). https://doi.org/10.1016/j.matdes.2016.12.048

23. V. Sklenicka, J. Dvorak, Effect of equal channel angular pressing (ECAP) on creep in aluminum alloy. Mater. Sci. Forum **539–543**, 2904–2909 (2007)

24. M. Omori, Sintering, consolidation, reaction and crystal growth by the spark plasma system (SPS). Mater. Sci. Eng. A **287**(2), 183–188 (2000)

25. D. Liu, Y. Chu, S. Jing, B. Ye, X. Zhou, Low-temperature synthesis of ultrafine TiB$_2$ nanopowders by molten-salt assisted borothermal reduction. J. Am. Ceram. Soc. **101**, 5299–5303 (2018). https://doi.org/10.1111/jace.15958

26. C. Beliciu, C. Moraru, Effect of solvent and temperature on the size distribution of casein micelles measured by dynamic light scattering. J. Dairy Sci. **92**(5), 1829–1839 (2009)

27. A.H. Kim, K.J. Seo, T. Kim, B. Lee, Nanometrology and its perspectives in environmental research. Environ. Health Toxicol. **29**, e2014016 (2014)

28. S. Saha, M. Ghosh, A. Kumar Pramanick, C. Mondal, J. Maity, Attainment of high specific hardness and specific modulus in spark plasma sintered aluminum-copper-silicon carbide-titanium carbide hybrid composite. Mater. Werkst. **52**(9), 965–981 (2021). https://doi.org/10.1002/mawe.20210010

29. B.D. Long, R. Othman, H. Zuhailawati, M. Umemoto, Comparison of two powder processing techniques on the properties of Cu-NbC composites. Adv. Mater. Sci. Eng. **2014**, 6 (2014)

30. B. Abdullah, D. Tahir, Quantitative analysis of X-Ray diffraction spectra for determine structural properties and deformation energy of Al, Cu and Si. J. Phys. Conf. Ser. **1317**, 012052 (2019)

31. S.J. Dong, Y. Zhou, Y.W. Shi, B.H. Chang, Formation of a TiB$_2$-reinforced copper-based composite by mechanical alloying and hot pressing. Metall. Mater. Trans. A **33**, 1275–1280 (2002)

32. C.M. Laursen, S.A. De Jong, S.M. Dickens, A.N. Exil, D.F. Susan, J.D. Carroll, Relationship between ductility and the porosity of additively manufactured AlSi10Mg. Mater. Sci. Eng. A **795**, 139922 (2020). https://doi.org/10.1016/j.msea.2020.139922

33. J.Z. Yi, Y.X. Gao, P.D. Lee, H.M. Flower, T.C. Lindley, Scatter in fatigue life due to effects of porosity in cast A356–T6 aluminum-silicon alloys. Metall. Mater. Trans. A **34**, 1879 (2003). https://doi.org/10.1007/s11661-003-0153-6

34. I.M. Makena, M.B. Shongwe, R. Machaka Mosimanegape, S. Masete, Effect of spark plasma sintering temperature on the pore characteristics, porosity and compression strength of porous titanium foams. SN Appl. Sci. **2**, 516 (2020). https://doi.org/10.1007/s42452-020-2258-6

35. M. Pellizzari, G. Cipolloni, Spark plasma sintering of copper matrix composites reinforced with TiB$_2$ particles. Materials **13**, 2602 (2020). https://doi.org/10.3390/ma13112602

36. U. Anselmi-Tamburini, J.E. Garay, Z.A. Munir, Fundamental investigations on the spark plasma sintering/synthesis process III. Current effect on reactivity. Mater. Sci. Eng. A **407**(1–2), 24–30 (2005)

37. U. Anselmi-Tamburini, Y. Kodera, M. Gasch, C. Unuvar, Z.A. Munir, M. Ohyanagi, S.M. Johnson, Synthesis and characterization of dense ultra-high temperature thermal protection materials produced by field activation through spark plasma sintering (SPS): I. Hafnium diboride. J. Mater. Sci. **41**(10), 3097–3104 (2006)

38. V. Viswanathan, T. Laha, K. Balani, A. Agarwal, S. Seal, Challenges and advances in nanocomposite processing techniques. Mater. Sci. Eng. R Rep. **54**, 121–285 (2006)

39. J. Adachi, K. Kurosaki, M. Uno, S. Yamanaka, Porosity influence on the mechanical properties of poly-crystallinezirconium nitride ceramics. J. Nucl. Mater. **358**, 106–110 (2006)

40. P. Yadav, A. Ranjan, H. Kumar, A. Mishra, J. Yoon, A contemporary review of aluminium MMC developed through stir-casting route. Materials **14**, 6386 (2021). https://doi.org/10.3390/ma14216386

41. A. Dey, K.M. Pandey, Magnesium metal matrix composites: a review. Rev. Adv. Mater. Sci. **42**, 58–67 (2015)

42. R.M. German, Sintering theory and practice, (Wiley, New York, 1996), pp. 568